PHYSICAL REVIEW B VOLUME 21, NUMBER 8 15 APRIL 1980

X-ray scattering study of one-dimensional lattice dynamics in $Hg_{3-\delta}AsF_6$

R. Spal,* C.-E. Chen,* T. Egami,† P. J. Nigrey, and A. J. Heeger*
Laboratory for Research on the Structure of Matter, University of Pennsylvania, Philadelphia, Pennsylvania 19104
(Received 9 October 1979)

The diffuse scattering of x rays by the linear chains of Hg atoms in the quasi-one-dimensional compound $Hg_{3-\delta}AsF_6$ was studied at temperatures from 100 to 350 K, and wave vectors from 7 to 20 $Å^{-1}$. The results are consistent with thermal diffuse scattering from a disordered one-dimensional "liquid" and, at high temperatures, agree quantitatively with the model of classical, independent, harmonic chains proposed by Emery and Axe. Deviations are observed in the temperature region from 130 to 200 K where the correlation length is about 25% longer than predicted.

I. INTRODUCTION

While thermal or quantum fluctuations are known to destroy long-range order in a strictly one-dimensional system, these fluctuations are easily suppressed in a quasi-one-dimensional system by weak transverse interactions, thus restoring long-range order. The quasi-one-dimensional metal $Hg_{3-\delta}AsF_6$ is the only known compound in which interchain interactions are sufficiently weak that the reduced dimensionality actually prevents long-range order in the crystal lattice. Thus, this remarkable compound makes possible, for the first time, the experimental study of one-dimensional lattice dynamics.

Several scattering studies of $Hg_{3-\delta}AsF_6$ have been reported. The original structural investigation by x rays[1] and later by neutrons[2] identified diffuse sheets of scattering intensity as Bragg scattering from independent, one-dimensional Hg chains. Subsequent neutron studies[3-5] revealed a one-dimensional phonon dispersion for longitudinal vibrations of the Hg chains, short-range order developing between chains below 180 K, and a phase ordering phase transition at 120 K establishing long-range order among the chains. A microscopic model of the lattice dynamics of weakly coupled chains has been developed by Emery and Axe[6] to account for the absence of order at high temperatures and the onset of short- and long-range order at low temperatures. In addition, the theory predicted a finite width for the scattering sheets. Due to the $1D$ lattice dynamics, the sheets do not arise from elastic Bragg scattering from independent, ordered $1D$ chains, but rather result from inelastic thermal diffuse scattering from a disordered $1D$ "liquid". The finite sheet width was subsequently observed by neutron scattering,[7] with the measured widths about 20% less than those predicted.

In the present study, the static structure factor $S(q)=\int d\omega\, S(q,\omega)$ was measured at various temperatures, primarily in the disordered phase, by EDXD (energy dispersive x-ray diffractometry).[8,9] Compared to neutron scattering, x-ray scattering has the advantage of directly measuring $S(q)$ rather than $S(q,\omega)$. Compared to conventional angular-scanning x-ray diffractometry, EDXD has the advantages of sampling a larger region of reciprocal space, and of scanning all parts of that region simultaneously.

This paper is divided as follows: Section II contains the derivation of $S(q)$, the experimental details are described in Sec. III, the data analysis is given in Sec. IV, and the principal results are presented and discussed in Sec. V. A summary and conclusion are given in Sec. VI.

II. $S(q)$ OF INDEPENDENT CHAINS

The structure factor is defined as follows:

$$S(q)=\frac{1}{N}\left\langle \sum_{l,m} e^{-iq(x_l-x_m)} \right\rangle, \tag{1}$$

where x_l is the position of the lth atom in a chain of N atoms, and the brackets denote a thermal average. The special case of a nearest-neighbor harmonic potential, treated classically, has been considered previously.[6] Since anharmonicity could be important at high temperatures, we will generalize the classical calculation of $S(q)$ to the case of an arbitrary nearest-neighbor symmetric potential. The restriction to a symmetric potential, $V(x)=V(-x)$, is justified since experiments have shown[4] that there is no thermal expansion in the Hg chains. Furthermore, we generalize the classical calculation to include the contribution from next-nearest-neighbor coupling. Finally, since the experiments described in this paper cover the temperature range well below the $1D$ Debye temperature, we include a quantum-mechanical derivation of $S(q)$ in the special case of a harmonic potential. In each case, we derive in addition $\langle (u_l-u_m)^2\rangle$ (where u_l is the displacement of the lth

atom from its equilibrium position) since this quantity is a natural measure of the disorder in the chain.

The Hamiltonian for a $1D$ lattice of N atoms with mass M interacting through first (V_1)- and second (V_2)-nearest-neighbor potentials is

$$H=\sum_i \frac{p_i^2}{2M}+V_1(x_{i+1}-x_i-d)+V_2(x_{i+2}-x_i-2d), \quad (2)$$

where x_i and p_i are the position and momentum of the ith atom, and d is the equilibrium separation between atoms. For $Hg_{3-\delta}AsF_6$, $M=200.6$ amu and $d=2.66$ Å.

To illustrate the effects of anharmonicity, let V_1 be symmetric, but otherwise arbitrary, and $V_2=0$. As shown in Appendix A,

$$S(q)=\frac{1-Z^2}{1+Z^2-2Z\cos qd} \quad (3)$$

and

$$\langle(u_l-u_m)^2\rangle=-|l-m|\,d^2Z/dq^2|_{q=0}, \quad (4)$$

where

$$Z(q)=\frac{\int dx \exp[iqx-\beta V_1(x)]}{\int dx \exp[-\beta V_1(x)]}. \quad (5)$$

Note that Z is real since V_1 is symmetric. Equations (3) and (4) each imply that there is no long-range order in the chain, since $S(\infty)=1$ and $\lim_{n\to\infty}\langle(u_{l+n}-u_l)^2\rangle=\infty$. In the special case of the harmonic potential $V_1(x)=\frac{1}{2}Mc^2(x/d)^2$, where c is the velocity of sound along the chain (for $Hg_{3-\delta}AsF_6$ at room temperature, neutron measurements[7] give $c=3.6\times10^5$ cm/sec), Eqs. (3), (4), and (5) reduce to

$$Z(q)=e^{-(1/2)\sigma^2q^2}, \quad (6)$$

$$\langle(u_l-u_m)^2\rangle=|l-m|\sigma^2, \quad (7)$$

and

$$S(q)=\frac{\sinh\frac{1}{2}\sigma^2q^2}{\cosh\frac{1}{2}\sigma^2q^2-\cos qd}, \quad (8)$$

where $(\sigma/d)^2\equiv k_BT/Mc^2$, in agreement with the results of Emergy and Axe.[6] For $Hg_{3-\delta}AsF_6$ at room temperature, $(\sigma/d)^2\sim10^{-3}$, implying a "correlation length" of about 10^3 lattice constants [see Eq. (7)]. Figure 1 compares $S(q)$ at room temperature for the harmonic potential [using Eq. (8)] and for the anharmonic potential $V_1(x)=\frac{1}{2}Mc^2[(x/d)^2+10^2(x/d)^4]$ [using Eqs. (3) and (5)]. As expected, the increased stiffness of the anharmonic potential leads to narrower structure in $S(q)$.

The effect of next-nearest-neighbor coupling is demonstrated by considering the extended harmonic potential with $V_1(x)=\frac{1}{2}Mc^2(x/d)^2$ and $V_2(x)=\alpha/2Mc^2(x/d)^2$ where α is assumed to be a small

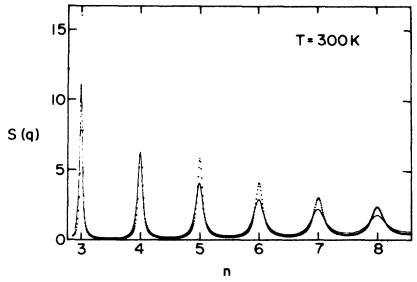

FIG. 1. Theoretical $S(q)$ vs n at 300 K. Solid curve assumes harmonic potential $\frac{1}{2}Mc^2(x/d)^2$, dotted curve assumes anharmonic potential $\frac{1}{2}Mc^2[(x/d)^2+10^2(x/d)^4]$.

quantity. Because the phonon dispersion relation is modified,

$$\omega(q)=(2c/d)(\sin^2\tfrac{1}{2}qd+\tfrac{1}{4}\alpha\sin^2qd)^{1/2}$$

the velocity of sound is increased to $(1+\alpha)^{1/2}c$. As shown in Appendix B, for $\alpha\ll1$:

$$\langle(u_l-u_m)^2\rangle=\sigma^2[(1-4\alpha)|l-m|+2\alpha] \quad (l\neq m) \quad (9)$$

and

$$S(q)=e^{-\alpha\sigma^2q^2}\frac{\sinh[\frac{1}{2}(1-4\alpha)]\sigma^2q^2}{\cosh[\frac{1}{2}(1-4\alpha)]\sigma^2q^2-\cos qd}+(1-e^{-\alpha\sigma^2q^2}). \quad (10)$$

Comparison of Eqs. (8) and (10) shows that the primary effect of the next-nearest-neighbor interaction is to multiply the structure factor by a slowly varying function.

Finally, we consider the quantum limit in the case of nearest-neighbor harmonic interaction [$V_1(x)=\frac{1}{2}Mc^2(x/d)^2$ and $V_2(x)=0$]. As shown in Appendix C, at $T=0$,

$$\langle(u_l-u_m)^2\rangle\cong\frac{d^2}{2\pi}\frac{k_B\Theta}{Mc^2}\ln|l-m| \quad (11)$$

and

$$S(q)\cong1+2\sum_{n=1}n^{-(d^2/4\pi)(k_B\Theta/Mc^2)q^2}\cos nqd, \quad (12)$$

where $\Theta\equiv2\hbar c/k_Bd\cong215$ K is the effective Debye temperature of the chains. These equations show that, as a result of zero-point motion, there is no long-range order even at $T=0$. From Eq. (12), $S(2\pi n/d)=\infty$, when $n\leq[(1/\pi)Mc^2/k_B\Theta]^{1/2}\simeq21$. However, although $S(q)$ diverges on the low-order sheets at $T=0$, the divergence is not a δ function with infinitesimal width, as would be the case if there were long-range order. While the zero-temperature limit is of interest, our experimental study is confined to $T/\Theta\gtrsim\frac{1}{2}$. As shown in Appendix C, in this regime inclusion of the leading quantum corrections gives

$$\langle(u_l-u_m)^2\rangle\cong\sigma^2[|l-m|+\tfrac{1}{24}(\Theta/T)^2] \quad (l\neq m) \quad (13)$$

and

$$S(q)=\exp\left[-\tfrac{1}{48}\left(\frac{\Theta}{T}\right)^2\sigma^2q^2\right]\frac{\sinh\tfrac{1}{2}\sigma^2q^2}{\cosh\tfrac{1}{2}\sigma^2q^2-\cos qd}+\{1-\exp[-\tfrac{1}{48}(\Theta/T)^2\sigma^2q^2]\}. \quad (14)$$

Since $qd\leq 16\pi$ in this study, Eq. (14) shows that corrections due to quantum effects are expected to be less than 10%.

The structure factor in Eqs. (3), (10), and (14) is of the general form

$$S(q)=A(q)\frac{1-Z^2}{1+Z^2-2Z\cos qd}+B(q), \quad (15)$$

where $A(q)$, $Z(q)$, and $B(q)$ all vary slowly over a given sheet. Thus, they may be replaced by their values at the center of that sheet, giving the expression

$$S(q)\simeq A_n\frac{1-Z_n^2}{1+Z_n^2-2Z_n\cos qd}+B_n \quad (16)$$

for $|qd-2n\pi|<\pi$ where $A_n\equiv A(2\pi n/d)$, $Z_n\equiv Z(2\pi n/d)$, and $B_n\equiv B(2\pi n/d)$. Consequently, in the data analysis (Sec. V) we use this general form for $S(q)$.

III. EXPERIMENTAL DETAILS

The energy dispersive x-ray diffractometer consisted of a Cu x-ray tube, operating at 50 kV and 14 mA; an intrinsic Ge detector, with a resolution of 150 eV at 5.9 keV and 475 eV at 122 keV; and a multichannel pulse-height analyzer (1024 channels) operating with a resolution of 50 eV/channel. The tube and detector were mounted on a vertical semicircular arc, which defined the scattering plane. At the center of the arc, the sample was mounted on a temperature-controlled stage inside a vacuum chamber with Be windows. Slits limited the divergence of the incident and scattered beams to about 0.2° in the scattering plane, and 0.8° perpendicular to the plane.

The sample was cut to expose a bc surface (the chain directions are $\hat{a}$ and $\hat{b}$), and mounted in the reflection geometry, with the incident and scattered beams forming angles of $\theta\cong 27°$ with the bc surface. By slightly tilting the sample until the $(2h,0,0)$ Bragg peaks appeared, the scattering vector was aligned precisely along $\hat{a}^*$. Finally, to avoid interference between the Bragg peaks and the sheets, the sample was rotated slightly to bring the scattering vector into the a^*c^* plane, 2.2° away from $\hat{a}^*$.

The temperature-controlled stage was heated by an electric heater, and cooled by a copper coil through which cold N_2 gas flowed. The temperature was monitored by a thermocouple, and was stable to ±1 K.

IV. DATA ANALYSIS

The experimental scattering intensity, $I_{\text{expt}}(E)$, is related to $S(q)$ as follows:

$$I_{\text{expt}}(E)=R(E)*I'_{\text{expt}}(E), \quad (17)$$

$$I'_{\text{expt}}(E)=C(E)[S(q)f_{\text{Hg}}^2(q)+I_C(q)], \quad (18)$$

$$C(E)=[P(E)/\mu(E)][k_\perp(E)+k_\parallel(E)\cos^2\theta], \quad (19)$$

where $q=(4\pi/\hbar c)E\sin\theta$, R is the diffractometer resolution profile, the operation * is a convolution, I'_{expt} is the experimental scattering intensity without resolution broadening, f_{Hg} is the atomic scattering factor of Hg, I_C is the Compton scattering intensity of the sample, C is the correction factor appropriate to the reflection geometry, P is the incident beam intensity, $k_\perp$ and $k_\parallel$ are the incident beam polarizations perpendicular and parallel to the scattering plane, and μ is the linear absorption coefficient of the sample. In the data analysis, we first determine $C(E)$ and subsequently correct for resolution broadening.

The correction factor C was determined experimentally by measuring I_{expt} of liquid Hg and solving Eq. (18) for C, using tabulated values of f_{Hg}, and using the approximations $S_{\text{Hg}}(q)\cong 1$ (which is valid for liquid Hg in the range $q\geq 7$ Å^{-1} used in this study) and $I_C(q)\cong[80-f_{\text{Hg}}(q)]^2$.[10] While μ, and hence C, are not the same for Hg and $Hg_{3-\delta}AsF_6$, $C_{Hg_{3-\delta}AsF_6}\cong AC_{\text{Hg}}$, since absorption by $Hg_{3-\delta}AsF_6$ is predominantly due to Hg (A is a constant determined by the relative densities of Hg and $Hg_{3-\delta}AsF_6$.) After I_{expt} was reduced to the form

$$I_{\text{red}}(q)\equiv\frac{I_{\text{expt}}(E)}{C(E)f_{\text{Hg}}^2(q)}=S(q)+I_C(q)/f_{\text{Hg}}^2(q), \quad (20)$$

the nth sheet of I_{red}, defined as the region $|qd-2n\pi|\leq\pi$, was fit by the method of nonlinear least squares to the function

$$I_{\text{fit}}(q)=A_n\frac{1-Z_n^2}{1+Z_n^2-2Z_n\cos(q-Q_n)d}+B_nq+C_n \quad (21)$$

yielding values of the five parameters Z_n, Q_n, A_n, B_n, and C_n, and their standard deviations. Since each sheet contained 105 data points, the least-squares fit had 100 degrees of freedom. Note that the only difference between Eqs. (16) and (21) is the inclusion of the parameters Q_n and C_n. The parameter Q_n corrects for any electronically introduced zero offset in the energy scale of the multichannel analyzer. Within experimental error, we find $Q_{n+1}-Q_n=2\pi/d$ where d is the experimentally determined equilibrium distance. The parameter C_n allows the "background" under a sheet to be a linear function of q, in order to adequately represent the slowly varying function I_C/f_{Hg}^2.

After making the nonlinear least-squares fits to Eq. (21), the quantities Z_n were corrected for resolution broadening, which is determined by the detector characteristics and the geometrical optics. The detector resolution profile is a Gaussian with a FWHM (full width at half maximum) of $\delta E_d = (a + bE)^{1/2}$, where a and b are constants which were determined from measured widths at 5.9 and 122 keV. The optical resolution profile is assumed to be also Gaussian, with a FWHM of $\delta E_0 = cE$, where c is a constant. Thus, the full resolution profile is Gaussian, with a FWHM of $\delta E = (\delta E_d^2 + \delta E_0^2)^{1/2}$. By measuring δE of four Bragg peaks, ranging from the third to the sixth sheet, the relation $\delta E_0 = cE$ was verified and a value and standard deviation of c was determined. This value agreed closely with that calculated from the geometrical optics. The parameter Z_n was corrected for resolution broadening by the following three steps: (1) The sheet was transformed into an equivalent Gaussian, with a FWHM of $W(Z_n)$, where $W(Z)d \equiv 2\arccos[2Z/(Z^2+1)]$, (2) the resolution broadening was removed, leaving a Gaussian with a FWHM of $[W(Z_n)^2 - \delta E^2]^{1/2}$, and (3) the Gaussian was transformed back to an equivalent sheet, with a corrected Z_n given by $W^{-1}[W(Z_n)^2 - \delta E^2)^{1/2}]$, where W^{-1} is the functional inverse of W. The basis for equivalence between a sheet with the parameter Z_n and a Gaussian with a FWHM of $W(Z_n)$ is the following observation: The first term in Eq. (21) has a maximum at $q = Q_n$ with minima at $q = Q_n \pm \pi/d$, and assumes a value halfway between its maximum and minima at $q = Q_n \pm \frac{1}{2}W(Z_n)$, so it resembles a Gaussian with a FWHM of $W(Z_n)$. Any errors introduced by assuming Gaussian line shapes in making the resolution corrections are expected to be small.

V. RESULTS AND DISCUSSION

Data were collected on the third through the eighth sheets, at temperatures ranging from 106 to 353 K. Typical counting rates and total counts at the center of a sheet were 0.1 counts/channel/sec and 5000 counts/channel, where 1 channel $\cong 0.025$ Å^{-1}. Figure 2 shows the raw data I_{expt} at 300 K and the corresponding reduced data I_{red}. The resemblance between $I_{\text{red}}(q)$ and $S(q)$ (see Fig. 1) is clear. Figure 3 shows the fitted data I_{fit} superimposed on I_{red} from Fig. 2. There are small discontinuities between the sheets because each sheet was fitted independently of the others. Finally, Fig. 4 illustrates the temperature variation of some fitted sheets.

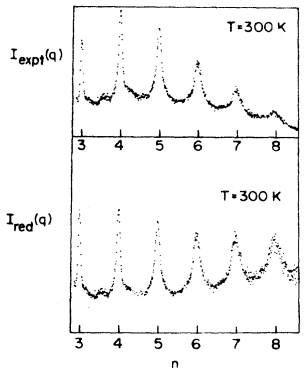

FIG. 2. $I_{\text{expt}}(q)$ and $I_{\text{red}}(q)$ vs n at 300 K.

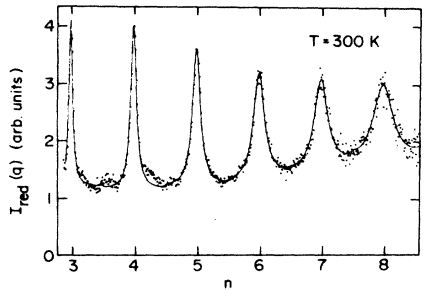

FIG. 3. $I_{\text{red}}(q)$ (data points) vs n at 300 K. The solid curve is $I_{\text{fit}}(q)$.

The results are presented, and simultaneously compared to the independent, harmonic chain model, in Figs. 5 and 6 and Table I. The comparison is facilitated by presenting the results in terms of the quantity $u_n(T)$:

$$u_n(T) \equiv -2\frac{Mc^2}{k_B T}\frac{1}{(2\pi n)^2}\ln Z_n(T). \tag{22}$$

For the harmonic potential, $u_n(T) = 1$ independent of n and T [see Eq. (6)]. Figure 5 is a graph of $Tu_n(T)$ vs n for two temperatures, and Fig. 6 is a graph of $nu_n(T)$ vs T for two sheets. The distance between the error bars in these figures is two

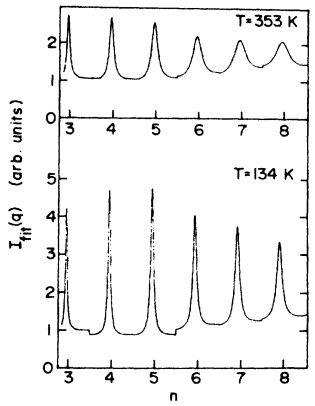

FIG. 4. I_{fit} (q) vs n at 353 K (upper curve) and 134 K (lower curve), with same units on both curves.

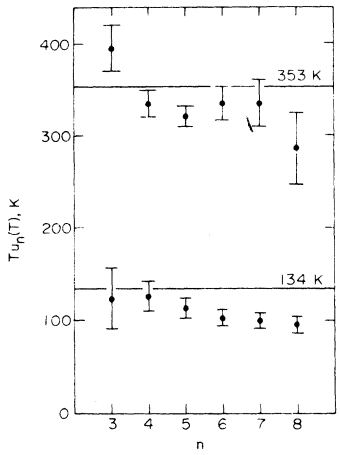

FIG. 5. $Tu_n(T)$ vs n at 353 K (upper data points) and 134 K (lower data points). Distance between error bars is two standard deviations. Solid lines represent nearest-neighbor harmonic theory.

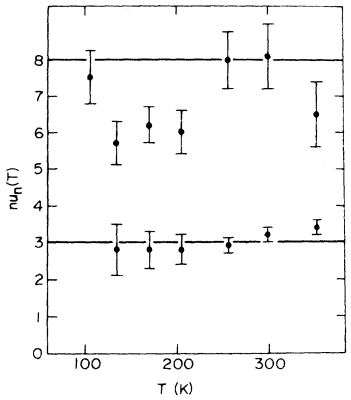

FIG. 6. $nu_n(T)$ vs T for $n=8$ (upper data points) and $n=3$ (lower data points). Distance between error bars is two standard deviations. Solid lines represent nearest-neighbor harmonic theory.

standard deviations. Table I gives, for all n and T, $u_n(T)$, the standard deviation of $u_n(T)$, and the number of standard deviations by which $u_n(T)$ differs from 1. In Figs. 7 and 8, the x-ray results are compared to those obtained from neutron scattering.[7] A direct comparison of $-(1/d)\ln Z_n$ with the parameter Γ_n in the neutron study is appropriate because, for a nearest-neighbor harmonic potential,

$$-(1/d)\ln Z_n = \frac{2\pi^2}{d}\frac{k_B T}{Mc^2}n^2 \equiv \Gamma_n .$$

Unlike Z_n, which depends only on the shape of I_{red}, A_n depends on the magnitude of I_{red}, which is determined by the relative number of scattering Hg atoms in the $Hg_{3-\delta}AsF_6$ sample and in the liquid-Hg sample used to determine $C(E)$. Although this makes accurate absolute measurements of A_n difficult, it does not affect the relative values of A_n for different n or T. The A_n were found to be temperature independent. For example, $A_7 = 0.96 \pm 0.03$ from 106 to 353 K. According to Eq. (10), if there were a significant next-nearest-neighbor interaction, A_n would be temperature dependent; the absence of such dependence implies that $\alpha < 0.02$. While A_n was independent of temperature, it did depend significantly on n, especially for small n. For example, typical values were A_3

TABLE I. Experimental values of $u_n(T)$ [see Eq. (22)] for n = 3 through 8 at various temperatures. The lower number in each entry is the number of standard deviations of the experimental value from $u_n(T) = 1$.

n: T	3	4	5	6	7	8
353	1.11 ± 0.06	0.95 ± 0.03	0.92 ± 0.03	0.95 ± 0.04	0.95 ± 0.07	0.82 ± 0.11
	1.8	−1.7	−2.7	−1.3	−0.7	−1.6
299	1.06 ± 0.05	1.02 ± 0.03	0.96 ± 0.03	0.95 ± 0.04	0.84 ± 0.05	1.02 ± 0.10
	1.2	0.7	−1.3	−1.3	−3.2	0.2
256	0.93 ± 0.07	[b]	0.91 ± 0.03	0.84 ± 0.03	0.91 ± 0.05	1.01 ± 0.09
	−1.0		−3.0	−5.3	−1.8	0.1
205	0.90 ± 0.10	[b]	0.81 ± 0.04	0.77 ± 0.04	0.76 ± 0.06	0.76 ± 0.06
	−1.0		−4.8	−5.8	−4.0	−4.0
170	0.88 ± 0.12	1.09 ± 0.05	0.86 ± 0.04	0.77 ± 0.04	0.75 ± 0.04	0.79 ± 0.05
	−1.0	1.8	−3.5	−5.8	−6.3	−4.2
134	0.83 ± 0.18	0.93 ± 0.07	0.85 ± 0.05	0.79 ± 0.04	0.76 ± 0.04	0.73 ± 0.05
	−0.9	−1.0	−3.0	−5.3	−6.0	−5.4
106	[a]	0.74 ± 0.18	[b]	0.99 ± 0.08	0.93 ± 0.07	0.94 ± 0.09
		−1.4		−0.1	−1.0	−0.7

[a] Sheet much narrower than resolution.
[b] Sheet obscured by overlapping $(2h+1, 0, 1)$ Bragg peak.

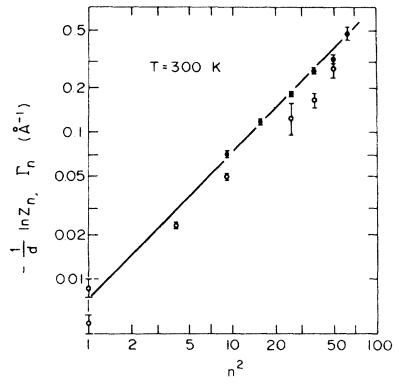

FIG. 7. $-(1/d)\ln Z_n$, Γ_n vs n^2 at 300 K. Solid circles are x-ray data, open circles are neutron data. Solid line represents nearest-neighbor harmonic theory.

$=0.5$, $A_5=0.9$, and $A_8=1.0$. This behavior is attributed to absorption of x rays by a thin oxide layer on the surface of the highly reactive sample, which was observed visually after the experiment. The relatively strong energy dependence of A_n for low energies (small n) is expected for an absorption effect.

The experimental results (see Table I and Figs. 5–8) may be summarized as follows: (1) The independent, harmonic-chain model is generally satisfactory, except when $134 \leq T \leq 205$ K and simultaneously $6 \leq n \leq 8$, in which case $u_n(T)$ consistently deviates from unity by more than three standard deviations and (2) when significant deviations occur, $u_n(T)$ is about 25% less than 1, indicating longer correlations in the chain than predicted by the independent, harmonic-chain model.

Before discussing these deviations from the theory of the harmonic chain, it is appropriate to examine some nonstatistical sources of error. The replacement of $A(E)$ by A_n in the data analysis is justified only if $A(E)$ does not vary strongly over the width of a sheet. As indicated above, $A(E)$ varied quite slowly for $n \geq 5$; furthermore, the effect of the more rapid variation for $n < 5$ is partially compensated by the narrower sheet widths for small n. A second source of error is resolution broadening. The intrinsic width $W(Z_n)$ of many sheets is comparable to the resolution width δE. For example, at 134 K, the ratio $W(Z_n)/\delta E$ was 0.5 for $n=3$ and 1.5 for $n=8$. (The ratio is smaller for small n because, roughly speaking, $W(Z_n) \propto n^2$ while $\delta E \propto E$.) The uncertainty in the resolution correction is reflected by the relatively large standard deviation of $u_n(T)$ for small n and low T. Finally, a third source of error is overlap between the sheets and the $(2h+1, 0, 1)$ Bragg peaks which occurred between the third and sixth sheets, where the scattering vector crossed the line $(\xi, 0, 1)$. (Note that the $(2h, 0, 1)$ reflections are forbidden by symmetry.) The intensity of the peaks was less than that of the sheets, and the width was naturally narrower. When a peak occurred near the minimum between two sheets, the neighborhood of the peak was excluded from the fitting region; when it occurred near the center of a sheet, the sheet was not fitted. In summary, the error bars indicated in Figs. 5–8 and Table I provide a valid estimate of the uncertainty in the data points. Thus the deviations for $6 \leq n \leq 8$ and $134 \leq T \leq 205$ K appear to be significant.

While the origin of these deviations from the independent, harmonic-chain model is not understood, examination of related structural data on $Hg_{3-\delta}AsF_6$ suggests that perhaps it is coupling between parallel chains. In this same temperature region, such coupling produces short-range order between parallel chains.[3,4] Although this order has only been observed as an intensity modulation in the first sheet along the line $(3-\delta, \eta, 0)$ it is plausible that the effects of the coupling might ap-

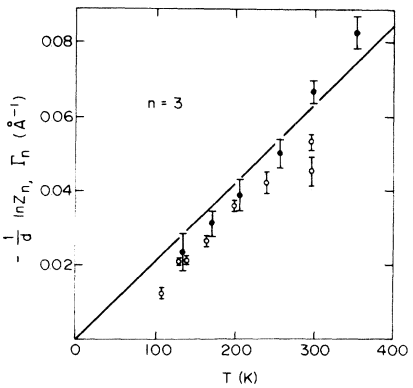

FIG. 8. $-(1/d)\ln Z_n$, Γ_n vs T for $n=3$. Solid circles are x-ray data, open circles are neutron data. Solid line represents nearest-neighbor harmonic theory.

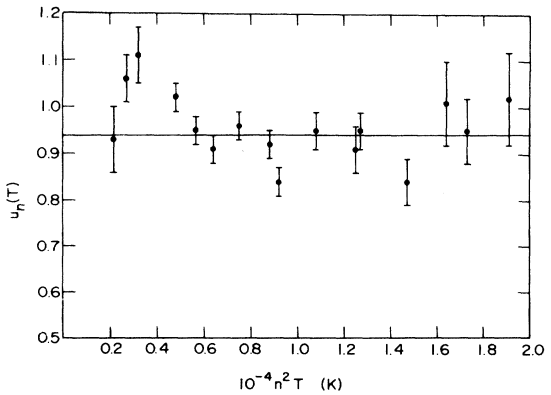

FIG. 9. $u_n(T)$ vs $10^{-4}n^2T$ for data above 250 K. Distance between error bars is two standard deviations. Solid line is the weighted average.

pear elsewhere in reciprocal space. Figure 9 plots the data from Table I in the restricted temperature range $T \geq 256$ K as $u_n(T)$ vs n^2T. Recall that for the classical harmonic chain, $u_n(T)=1$. The results in the high-temperature regime, where structural data indicate independent chains without significant interchain phase order, are in excellent agreement with the classical harmonic chain. The weighted average value, $\langle u_n(T)\rangle = 0.94 \pm 0.01$, suggests a velocity of sound about 3% greater than the value obtained from the inelastic neutron scattering experiments.

VI. SUMMARY

The one-dimensional lattice dynamics of the incommensurate linear Hg chains in $Hg_{3-\delta}AsF_6$ has been established through a detailed study of the thermal diffuse scattering. As a result of the weak interchain coupling, the Hg chains act as independent $1D$ chains and therefore do not exhibit long-range order, resulting in the finite width of the $1D$ scattering sheets. The experimental results are consistent with thermal diffuse scattering from a disordered $1D$ "liquid" and, at high temperatures, agree quantitatively with the model of classical, independent, harmonic chains proposed by Emery and Axe. Deviations are observed in the temperature region 130 to 200 K where the correlation length is about 25% longer than predicted.

ACKNOWLEDGMENTS

We thank Professor Alan G. MacDiarmid for advice and cooperation regarding the crystals used in this study, Professor Shlomo Alexander for suggesting the use of EDXD, and Dr. V. J. Emery for several helpful discussions on the origins of deviations from harmonic, classical behavior. This work was supported by the National Science Foundation, MRL Program, under Grant No. DMR76-80994.

APPENDIX A

Below, $\langle (u_l - u_m)^2\rangle$ and $S(q)$ are calculated in the classical limit for a nearest-neighbor, symmetric potential. These quantities may be conveniently obtained from the following thermal average:

$$\langle \exp[i(q_1u_1+\cdots+q_Nu_N)]\rangle = \int du_1\cdots du_N \exp[i(q_1u_1+\cdots+q_Nu_N)]\exp\{-\beta[V_1(u_1-u_0)+\cdots+V_1(u_N-u_{N-1})]\}$$
$$\times\left(\int du_1\cdots du_N \exp\{-\beta[V_1(u_1-u_0)+\cdots+V_1(u_N-u_{N-1})]\}\right)^{-1}$$
$$= \int dy_1\cdots dy_N \exp\{i[(q_1+\cdots+q_N)y_1+(q_2+\cdots+q_N)y_2+\cdots+q_Ny_N]\}$$
$$\times\exp\{-\beta[V_1(y_1)+\cdots+V_1(y_N)]\}\left(\int dy_1\cdots dy_N \exp\{-\beta[V_1(y_1)+\cdots+V_1(y_N)]\}\right)^{-1},$$

where $y_i \equiv u_i - u_{i-1}$ and $u_0 \equiv 0$.

$$\langle \exp[i(q,u,+\cdots+q_Nu_N)]\rangle = Z(q_1+\cdots+q_N)Z(q_2+\cdots+q_N)\cdots Z(q_N). \tag{A1}$$

Since $Z(q)=Z^*(q)=Z(-q)$ and $Z(0)=1$, setting $q_l=-q_m=q$ and $q_i=0$ $(i\neq l,m)$ gives

$$\langle e^{iq(u_l-u_m)}\rangle = Z^{|l-m|}, \tag{A2}$$

where $Z\equiv Z(q)$. Thus,

$$\langle (u_l-u_m)^2\rangle = -\frac{d^2}{dq^2}\langle e^{iq(u_l-u_m)}\rangle|_{q=0} = -\frac{d^2}{dq^2}Z^{|l-m|}\Big|_{q=0},$$
$$\langle (u_l-u_m)^2\rangle = -|l-m|\left.\frac{d^2Z}{dq^2}\right|_{q=0}. \tag{A3}$$

$$S(q) \equiv \lim_{n\to\infty}\frac{1}{N}\sum_{l=1}^{N}\sum_{m=1}^{N}\langle e^{iq(x_l-x_m)}\rangle = \lim_{N\to\infty}\frac{1}{N}\sum_{l=1}^{N}\sum_{m=1}^{N}e^{iqd(l-m)}Z^{|l-m|},$$
$$S(q) = \sum_{n=-\infty}^{\infty}e^{inqd}Z^{|n|} = \frac{1}{1-e^{iqd}Z}+\frac{1}{1-e^{-iqd}Z}-1, \tag{A4}$$
$$S(q) = \frac{1-Z^2}{1+Z^2-2Z\cos qd}.$$

APPENDIX B

Below, $\langle (u_l - u_m)^2 \rangle$ and $S(q)$ are calculated in the classical limit for a harmonic, next-nearest-neighbor potential. As before, these quantities may be conveniently obtained from the following thermal average:

$$\begin{aligned}\langle \exp[i(q_1u_1 + \cdots + q_Nu_N)] \rangle &= \int du_1 \cdots du_N \exp[i(q_1u_1 + \cdots + q_Nu_N)] \\ &\quad \times \exp\{-\beta[V_1(u_1 - u_0) + \cdots + V_1(u_N - u_{N-1}) + V_2(u_2 - u_0) + \cdots + V_2(u_N - u_{N-2})]\} \\ &\quad \times \left(\int du_1 \cdots du_N \exp\{-\beta[V_1(u_1 - u_0) + \cdots + V_2(u_N - u_{N-2})]\} \right)^{-1} \\ &= \int dy_1 \cdots dy_N \exp\{i[(q_1 + \cdots + q_N)y_1 + (q_2 + \cdots + q_N)y_2 + \cdots + q_Ny_N]\} \\ &\quad \times \exp\{-\beta[V_1(y_1) + \cdots + V_1(y_N) + V_2(y_1 + y_2) + \cdots + V_2(y_{N-1} + y_N)]\} \\ &\quad \times \left(\int du_1 \cdots du_N \exp\{-\beta[V_1(y_1) + \cdots + V_2(y_{N-1} + y_N)]\} \right)^{-1} \\ &= \int dy_1 \cdots dy_N \exp(i\vec{q} \cdot \vec{y}) \exp[-(1/2\sigma^2)\vec{y} \cdot \vec{A} \cdot \vec{y}] \left(\int dy_1 \cdots dy_N \exp[-(1/2\sigma^2)\vec{y} \cdot \vec{A} \cdot \vec{y}] \right)^{-1},\end{aligned}$$

where

$$\vec{q} \equiv \begin{pmatrix} q_1 + \cdots + q_N \\ q_2 + \cdots + q_N \\ \cdot \\ \cdot \\ \cdot \\ q_N \end{pmatrix}, \quad \vec{y} \equiv \begin{pmatrix} y_1 \\ \cdot \\ \cdot \\ \cdot \\ y_N \end{pmatrix},$$

and $\vec{A}$ is the $N \times N$ tridiagonal matrix

$$\begin{pmatrix} 1+2\alpha & \alpha & 0 & \cdots \\ \alpha & 1+2\alpha & \alpha & \\ 0 & \alpha & 1+2\alpha & \\ \cdot & & & \\ \cdot & & & \\ \cdot & & & \end{pmatrix}.$$

Since $\vec{A}$ may be diagonalized by a unitary transformation, it follows that

$$\langle \exp[i(q_1u_1 + \cdots + q_Nu_N)] \rangle = \exp(-\tfrac{1}{2}\sigma^2 \vec{q} \cdot \vec{A}^{-1} \cdot \vec{q}), \tag{B1}$$

where

$$A^{-1} \cong \begin{pmatrix} 1-2\alpha & -\alpha & 0 & \cdots \\ -\alpha & 1-2\alpha & -\alpha & \\ 0 & -\alpha & 1-2\alpha & \\ \cdot & & & \\ \cdot & & & \\ \cdot & & & \end{pmatrix}$$

since $\alpha \ll 1$. Setting $q_l = -q_m = q$ and $q_i = 0$ $(i \neq l, m)$ gives for $l \neq m$

$$\langle \exp[iq(u_l - u_m)] \rangle = \exp\{-\tfrac{1}{2}\sigma^2 q^2 [(1-2\alpha)|l-m| - 2\alpha(|l-m|-1)]\}. \tag{B2}$$

Thus,

$$\langle (u_l - u_m)^2 \rangle = [(1-4\alpha)|l-m| + 2\alpha]\sigma^2 \tag{B3}$$

and

$$S(q)=e^{-\alpha\sigma^2q^2}\frac{\sinh\frac{1}{2}(1-4\alpha)\sigma^2q^2}{\cosh\frac{1}{2}(1-4\alpha)\sigma^2q^2-\cos qd}+(1-e^{-\alpha\sigma^2q^2}). \tag{B4}$$

APPENDIX C

Below, $\langle(u_l-u_m)^2\rangle$ and $S(q)$ are calculated quantum mechanically for a harmonic, nearest-neighbor potential. The quantity $\langle(u_l-u_m)^2\rangle$ is given by the following integral:

$$\langle(u_l-u_m)^2\rangle=\frac{\hbar}{2MN}\sum_{p,q}\frac{1}{[\omega(p)\omega(q)]^{1/2}}(e^{ilpd}-e^{impd})(e^{ilqd}-e^{imqd})\langle(a_p+a_{-p}^{\dagger})(a_q+a_{-q}^{\dagger})\rangle$$

$$=\frac{2\hbar}{MN}\sum_q\frac{1-e^{i(l-m)qd}}{\omega(q)}[n(q)+\tfrac{1}{2}] \tag{C1}$$

$$=\frac{k_B\Theta}{Mc^2}\frac{d^2}{4\pi}\int_0^{\pi}dq\,\frac{1-e^{i(l-m)q}}{\sin\frac{1}{2}q}\coth\frac{\Theta}{2T}\sin\tfrac{1}{2}q\ , \tag{C2}$$

where $a_q^{\dagger}$ and a_q are phonon creation and destruction operators,

$$\omega(q)\equiv\frac{2c}{d}\sin|\tfrac{1}{2}qd|$$

and

$$n(q)\equiv\frac{1}{e^{\beta\hbar\omega(q)}-1}.$$

For $T=0$, evaluation of the integral gives

$$\langle(u_l-u_m)^2\rangle=\frac{k_B\Theta}{Mc^2}\frac{d^2}{\pi}\sum_{n=0}^{|l-m|-1}\frac{1}{2n+1}$$

$$\cong\frac{k_B\Theta}{Mc^2}\frac{d^2}{2\pi}\ln|l-m|, \tag{C3}$$

so that

$$S(q)=1+2\sum_{n=1}^{\infty}\cos nqd\,\exp[-\tfrac{1}{2}\langle(u_{l+n}-u_l)^2\rangle q^2]$$

$$\cong1+2\sum_{n=1}^{\infty}n^{-(1/4\pi)(k_B\Theta/Mc^2)q^2d^2}\cos nqd. \tag{C4}$$

Since $\coth x\cong1/x+\frac{1}{3}x$ for $x<1$, when $\Theta/2T<1$ evaluation of the integral gives

$$\langle(u_l-u_m)^2\rangle\cong\sigma^2[|l-m|+\tfrac{1}{24}(\Theta/T)^2] \tag{C5}$$

for $l\neq m$ and

$$S(q)\cong\exp[-\tfrac{1}{48}(\Theta/T)^2\sigma^2q^2]\,\frac{\sinh\frac{1}{2}\sigma^2q^2}{\cosh\frac{1}{2}\sigma^2q^2-\cos qd}$$

$$+\{1-\exp[-\tfrac{1}{48}(\Theta/T)^2\sigma^2q^2]\}. \tag{C6}$$

*Present address: Department of Physics, University of Pennsylvania, Philadelphia, Penn.

†Present address: Department of Materials Science and Engineering, University of Pennsylvania, Philadelphia, Penn.

[1]I. D. Brown, B. D. Cutforth, C. G. Davies, R. J. Gillespie, P. R. Ireland, and J. E. Vebries, Can. J. Chem. 52, 791 (1974).

[2]A. J. Schultz, J. M. Williams, N. D. Miro, A. G. MacDiarmid, and A. J. Heeger, Inorg. Chem. 17, 646 (1978).

[3]J. M. Hastings, J. P. Pouget, G. Shirane, A. J. Heeger, N. D. Miro, and A. G. MacDiarmid, Phys. Rev. Lett. 39, 23 (1977); 39, 1484 (1977).

[4]J. P. Pouget, G. Shirane, J. M. Hastings, A. J. Heeger, and A. G. MacDiarmid, Phys. Rev. B 18, 7 (1978); 18, 3645 (1978).

[5]I. U. Heilmann, J. M. Hastings, G. Shirane, A. J. Heeger, and A. G. MacDiarmid, Solid State Commun. 29, 6 (1979); 29, 469 (1979).

[6]V. J. Emery and J. D. Axe, Phys. Rev. Lett. 40, 23 (1978); 40, 1507 (1978).

[7]I. U. Heilmann, J. D. Axe, J. M. Hastings, G. Shirane, A. J. Heeger, and A. G. MacDiarmid, Phys. Rev. B 20, 751 (1979).

[8]J. M. Prober and J. M. Schultz, J. Appl. Crystallogr. 8, 405 (1975).

[9]T. Egami, J. Mater. Sci. 13, 2587 (1978).

[10]S. E. Rodriguez and C. J. Pings, Acta Crystallogr. 18, 979 (1965).